Influence of Post-Welding Heat Treatment on the Corrosion Behavior of a 2050-T3 Aluminum-Copper-Lithium Alloy Friction Stir Welding Joint

Vincent Proton, Joël Alexis, Eric Andrieu, Christine Blanc, Jérôme Delfosse, Loïc Lacroix, Grégory Odemer

Influence of Post-Welding Heat Treatment on the Corrosion Behavior of a 2050-T3 Aluminum-Copper-Lithium Alloy Friction Stir Welding Joint

Vincent Proton,[a] Joël Alexis,[b] Eric Andrieu,[a] Christine Blanc,[a,*,z] Jérôme Delfosse,[c] Loïc Lacroix,[b,*] and Grégory Odemer[a]

[a]*Université de Toulouse, CIRIMAT, UPS/CNRS/INPT, 4 allée Emile Monso BP 44362, 31030 Toulouse Cedex 04, France*
[b]*Université de Toulouse, LGP, ENIT, BP 1629, 65016 Tarbes Cedex, France*
[c]*EADS Innovation Works-IW/MS/MM, 12 rue Pasteur, BP 76, 92152 Suresnes Cedex, France*

The corrosion behavior of a Friction Stir Welding joint in 2050-T3 Al-Cu-Li alloy was studied in 1 M NaCl solution and the influence of T8 post-welding heat treatment on its corrosion susceptibility was analyzed. After exposure to 1 M NaCl solution, the heat affected zone (HAZ) of the weld without post-welding heat treatment was found to be the most extensively corroded zone with extended intergranular corrosion damage while, following T8 post-welding heat treatment, no intergranular corrosion was observed in the HAZ and the global corrosion behavior of the weld was significantly improved. The corrosion damage observed on the welded joints after immersion in 1 M NaCl solution was compared to that obtained after 750 h Mastmaasis Wet Bottom tests. The same corrosion damage was observed. Various stationary electrochemical tests were carried out on the global welded joint and/or each of the metallurgical zones of the welded joint to understand the corrosion damage observed. TEM observations helped in bringing meaningful elements to analyze the intrinsic electrochemical behavior of the different zones of the weld related to their microstructure. However, galvanic coupling tests showed that galvanic coupling effects between the different zones of the weld were at least partially responsible for its corrosion behavior.

[DOI: 10.1149/1.3562206]

When dealing with the design of metal aircraft structures, manufacturers have explored several solutions to reduce both the weight and the cost. Among the solutions, two are currently under consideration by the aircraft Industry. The first consists in substituting 7xxx aluminum alloys for aluminum-copper-lithium alloys. The density of these new-generation alloys is 3% lower when they contain just 1 wt% Li.[1] Moreover, their mechanical properties are similar to those of 7xxx alloys.[2] The second solution is to replace the riveting process currently used in the assembly of structural elements by Friction Stir Welding (FSW). The FSW process was developed by The Welding Institute (TWI) and consists of the use of a non-consumable cylindrical, rotating tool (usually hardened steel) which moves over the seam of two butted plates and stirs them together.[3] The combined use of Al-Cu-Li alloys and the FSW process is a strategic axis of development in the aeronautical industry so a better understanding of the properties of FSW structures is required.

Structural hardening of Al-Cu-Li alloys mainly results from intermetallic precipitates of three types i.e., Ω (Al_2Cu), T_1 (Al_2CuLi) and δ′ (Al_3Li) phases whose actual contribution depends on the Cu and Li content of the alloys.[4] Thus, the first order contribution to structural hardening is due to Ω precipitates for a Li content (wt%) lower than 0.6, T_1 for a Li content lower than 1.5 and δ′ for Li content greater than 1.5. The nucleation (and growth) of T_1 precipitates is heterogeneous so it occurs at grain and subgrain boundaries as well as on dislocations.[5] Gable et al. have demonstrated that plastic deformation before heat treatment involves an increase of the volume fraction of T_1 in the matrix.[6] Al-Cu-Li alloys also contain other intermetallic precipitates such as θ′ (Al_2Cu), T_2 (Al_5Li_3Cu) and T_B (Al_7Cu_4Li) which can also contribute to strengthening the alloy but to a lesser extent than those already mentioned.[7] Moreover, coarse intermetallic particles and dispersoids can also be observed in this complex microstructure. These aluminum alloys thus present a heterogeneous microstructure which can induce a susceptibility to corrosion. These alloys are, for instance, susceptible to pitting corrosion and intergranular corrosion in 3.5% NaCl.[8–10] Actually, some authors have studied the electrochemical behavior of the precipitates present in the alloy compared to that of the matrix.[11–13] They emphasized that the electrochemical behavior of T_1 precipitates changed over time during immersion in 4% NaCl. The T_1 precipitates, that were anodic towards the matrix at the beginning of the immersion test in 4% NaCl, became cathodic towards the matrix after approximately 50 h. The reports stated that it was the alternating dissolution of the T_1 precipitates and the matrix which led to the corrosion behavior observed. The authors also studied the cathodic behavior of the θ′ phase and the alternating cathodic and anodic behavior of T_2 towards the matrix.[11,13]

The FSW process leads to an increase of the temperature and severe plastic deformation around the weld. Whatever the aluminum alloy welded, a typical friction stir weld consists of unaffected base material (BM), a heat affected zone (HAZ), a thermo-mechanically affected zone (TMAZ) and a dynamically recrystallized zone (DXZ or nugget). The microstructure of each zone depends on the heat treatment and the plastic deformation generated during the welding process. Some authors have studied the microstructure of welded joints of Al-Cu-Li alloys. They showed that the welded joint obtained presented a microstructure gradient with a decrease of the volume fraction of T_1 precipitates from the BM to the TMAZ.[14,15] Precipitation in the nugget depended on many factors such as how fast the tool was spinning, its transverse speed and finally the thickness of the plate.[14,15] The microstructural differences between the various zones of the joint led to different mechanical behavior for each zone and particularly affected the ductility of the nugget, which is twice that of the base metal.[16] Concerning the electrochemical behavior of the welded joints, the global corrosion behavior of welded joints of Al-Cu-Li alloys in 3.5% NaCl was studied by Corral et al. who noticed that all the zones behave in the same way from a macroscopic point of view.[17] The global corrosion behavior of the weld in 3.5% NaCl was also studied by Hu and Meletis[18] who noticed that the joint was sensitive to a non-uniform pitting. Nevertheless, each zone seemed to be more resistant to corrosion than the base metal. Paglia and Buchheit observed that the HAZ, the TMAZ and the nugget were sensitive to intergranular and pitting corrosion.[19] Hu and Meletis[18] and Padgett et al.[20] also studied the specific electrochemical behavior of each zone in 3.5% NaCl. They showed that BM, HAZ, TMAZ and the nugget had different free potentials and corrosion potentials. As a consequence, when the weld was exposed to an aggressive environment, galvanic coupling could occur between the different zones. This galvanic coupling phenomenon was highlighted by Danford and Ding using the Scanning Reference Electrode Technique (SRET) on a FSW weld in a 3.5% NaCl solution.[21] They showed that the nugget presented a cathodic behavior with respect to the other zones of the weld. Lequeu et al. showed that the HAZ seemed to be more sensitive to intergranular corrosion than the other parts of the weld.[2]

* Electrochemical Society Active Member.
z E-mail: christine.blanc@ensiacet.fr

However, despite the aeronautic industry's growing interest for FSW joints of Al-Cu-Li alloys, it is worth noting that very few works concern their corrosion behavior. The present work aims to contribute to a better understanding of the corrosion behavior of welded Al-Cu-Li alloy joints. The weld studied was a FSW joint in 2050 Al-Cu-Li alloy. The material was welded in the T351 metallurgical state and submitted, after the welding process, to T8 heat treatment. The purpose of the present manuscript is to study the influence of post-welding heat treatment on the corrosion behavior of the FSW structure. The microstructure of the welded joint was first studied by optical microscopy (OM) combined with hardness measurements to identify the different metallurgical zones generated by the welding process. The corrosion behavior of the global welded joint and that of each individual zone of the weld were studied in 1 M NaCl solution by using stationary electrochemical tests (open circuit potential measurements, plotting of current-potential curves). The corrosion damage observed in 1 M NaCl solution was compared to that obtained after Mastmaasis Wet Bottom tests which is a frequently used industrial test. Combination between electrochemical results and transmission electron microscopy (TEM) observations performed for both metallurgical states, i.e., with or without the post-welding heat treatment, was helpful in correlating the corrosion behavior observed for each individual zone and for the global welded joint to their microstructure. However, comparison of the results obtained for the whole welded joint to those of each individual zone allowed some galvanic coupling phenomena to be revealed and galvanic coupling tests were performed to obtain further understanding of the corrosion behavior of the welded joint.

Experimental

Material.—15 mm thick plates of a 2050 Al-Cu-Li alloy (Al base, 1% Li, 3.55% Cu, 0.04% Si, 0.05% Fe, 0.35% Mn, 0.4% Mg, 0.12% Zn, 0.45% Ag, 0.1% Zr) were provided by Alcan CRV. The plates were obtained by hot rolling followed by solutionising, quenching and stretching leading to the so-called T3 metallurgical state. To obtain a weld joint, two plates were butt welded in the rolling direction (longitudinal L direction) by EADS IW using a conventional Friction Stir Welding (FSW) process. Half of the welds were submitted to a post-welding heat treatment (PWHT) which consisted of a T8 over-aged heat treatment. The welds without the post-welding heat treatment were called NHT. Finally, the assembly was milled down until the final thickness reached 11.5 mm.

Study of the corrosion behavior.—The corrosion behavior of each zone of the weld was studied with appropriate stationary electrochemical tests i.e., open circuit potential (OCP) measurements and plotting of current-potential curves. A three-electrode electrochemical cell was used including a platinum grid with a large surface area as the auxiliary electrode; the reference electrode was a saturated calomel electrode (SCE) with a Luggin capillary. All potentials quoted in the manuscript are with respect to the SCE reference. The electrolyte was a 1 M NaCl solution prepared by dissolving Normapur chemical salts in distilled water. For all experiments, the electrolyte was stirred, in contact with air and maintained at a temperature of 22°C using a Julabo refrigerated circulator. Before the tests, the samples were mechanically polished down to 4000 grit SiC paper and then down to 1 μm with a diamond paste, with distilled water as lubricant. Depending on the zone studied, the base metal (BM), the Heat Affected Zone (HAZ) and the nugget were insulated with varnish and the electrode surface area was accurately measured. The surface studied always corresponded to the L–LT plane at a depth of 6 mm from the top of the weld. OCP measurements were performed with a test duration of about 4000 s. To better understand the corrosion behavior of the weld, OCP measurements were also performed on the whole weld. Current-potential curves were also plotted; on the immersion of the sample in the electrolyte, the potential was immediately scanned at a rate of 500 mV h^{-1} from –1100 to –300 mV/SCE. The corrosion damage observed on the welds after exposure to 1 M NaCl solution was compared to that observed after a 750 h Mastmaasis Wet Bottom test performed in the EADS Suresnes laboratory.[22] This test consisted of alternative phases of spraying of acetic acid and saline solution and exposing to a wet atmosphere. It was performed on the freshly milled surface without other surface preparation. After the test, the corrosion damage of PWHT and NHT joints was characterized under the optical microscope. Finally, galvanic coupling tests were also carried out in 1 M NaCl solution between the different zones of the weld using a Zero Resistance Ammeter set up. For these tests, two cycles were applied with one cycle as follows: the two electrodes were first disconnected from each other and the OCP of both electrodes was measured for 10 min; then they were electrically connected and both the galvanic current and the OCP of the couple were measured for 2 h. After each electrochemical test, the sample surface was accurately observed.

Microscopic observations.—An Olympus PMG3 optical microscope was used to perform observations of the sample surface immediately after the corrosion tests to characterize the corrosion damage. For the Mastmaasis Wet Bottom tests, observations were performed on the sample surface just after the tests; additional observations were performed by cutting and mechanically polishing the sample down to 1 μm to observe the corrosion damage in the long transverse (LT)–short transverse (ST) plane. Optical microscopy was also used to characterize the microstructure of the different zones of the weld. To do so, Keller's metallographic etching (1 ml of hydrofluoric acid 40 wt%, 1.5 ml of hydrochloric acid 35 wt%, 2.5 ml of nitric acid 68 wt% and 95 ml of distilled water) was performed to reveal the grains. Additional information was obtained from TEM observations with a JEOL-JEM-2010. The samples were obtained by removing 300 μm thick slices from each zone of the weld. The slices were ground down to about 100 μm thick and a dimple was machined in the central region. Final electron transparency was obtained by ion milling on a precision ion polishing system [PIPS(tm), Gatan] using 5 kV Ar^{+} ions.

Mechanical behavior.—Vickers hardness was measured in the LT–ST plane at a depth corresponding to the center of the sheet. Hardness profiles were plotted across the welded joint using a load of 1 kg.

Results and Discussion

Microstructure.—Figure 1a shows an optical micrograph in the LT–ST plane of a PWHT welded joint after Keller's metallographic etching. The same observations were performed on a weld without the post-welding heat treatment but no difference was observed between the PWHT and the NHT joint at this scale of observation. The micrograph allows the different zones obtained after the welding process to be located. Figures 1b–1d give representative observations of each zone. The base metal (BM, Fig. 1b) presented elongated grains in the LT direction with an average grain size of 320 μm in the LT direction compared to 25 μm in the ST direction. Observations performed in other characteristic planes of the sheet allowed the grain size in the L direction to be measured; it was found to be close to an average size of 620 μm. Due to the FSW process, i.e., the friction phenomenon, a heat-affected zone (HAZ) was present. In this zone, modifications of the precipitation could be expected but this was not observed under optical microscopy. Closer to the nugget, a thermo-mechanically affected zone was encountered (Fig. 1c). It exhibited sheared grains due to tool rotation and was thus clearly visible on the micrograph. In the center of the welded joint, the nugget presented equiaxed grains, resulting from dynamic recrystallisation[23]; their average sizes varied from 16 μm in the upper surface to 4 μm in the lower surface (Fig. 1d). SEM observations of the different zones of the welded joint did not provide additional data.

Vickers hardness profiles measured across the welded joints showed that, for the NHT weld, Vickers hardness was nearly constant and equal to 95 Hv_1 right across the weld (Fig. 2). In contrast, for the PWHT weld, the hardness profile obtained showed that the hardness was very high in the base metal and then decreased in the

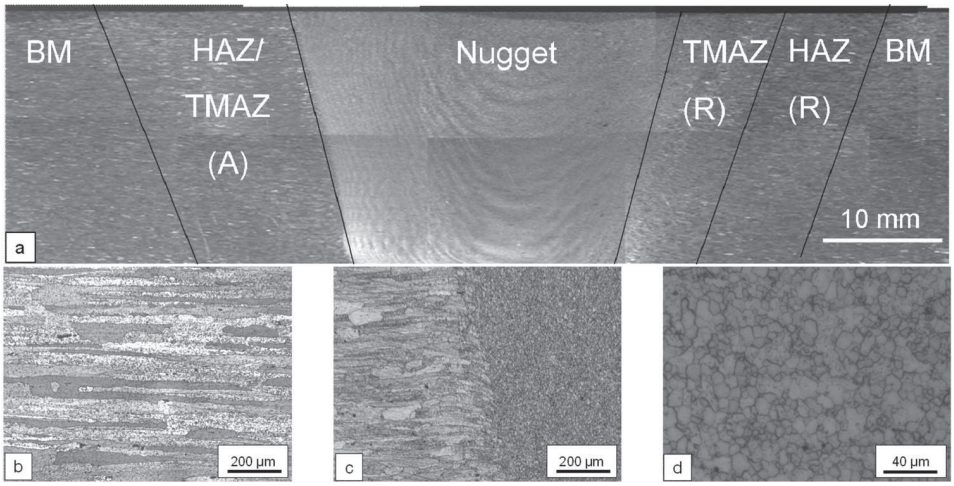

Figure 1. Optical observations after etching with Keller's solution of (a) a welded joint of 2050-T3 alloy submitted to a T8 post-welding heat treatment. Zoom on (b) the base metal (c) the TMAZ and (d) the nugget. (A) advancing side, (R) retreating side.

HAZ to finally reach a minimum value in the nugget. The variation of the hardness across the weld was related to precipitation but also to the dislocation density as explained later in the manuscript. The variations of the hardness across the welded joints were helpful in defining the borders limiting the different zones so that the corrosion behavior of each zone could be studied. Moreover, both optical observations and hardness measurements revealed and/or suggested significant differences in microstructure in terms of grain size and precipitation state between the different zones of a same weld but also between the weld with or without the post welding heat treatment. It was thus expected that galvanic coupling phenomena could appear between the different zones of a given weld depending on its heat treatment state.

Electrochemical tests in 1 M NaCl solution.—Experiments were performed in a 1 M NaCl electrolyte on the global welded joint and on each metallurgical zone of the weld. For OCP measurements performed on the global welded joint, a sample of welded joint was machined so that the total area of base metal exposed to the electrolyte was equal to the sum of the areas of the HAZ and the nugget. In a second set of experiments, each zone of the welded joint was insulated and both open circuit potential measurements and potentiokinetic polarizations were performed. Figure 3 shows the electrochemical results obtained for the NHT samples with OCP measurements for the BM, the HAZ, the nugget and the global welded joint (Fig. 3a), the potentiokinetic polarization curves plotted individually for the three

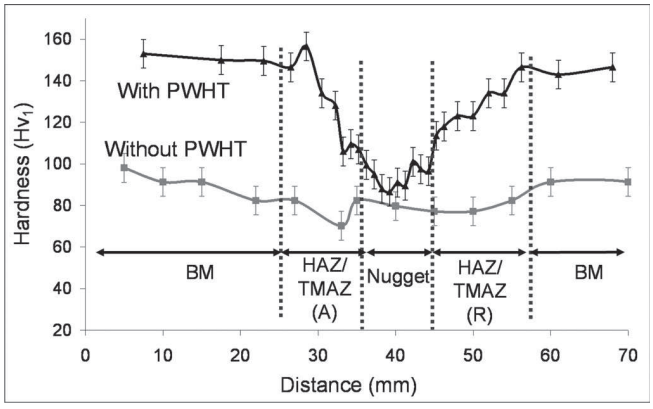

Figure 2. Vickers hardness profiles plotted in the LT–ST plane of FSW joints of the 2050-T3 alloy. The profiles were obtained in the centre of the sheet for the weld without post-welding heat treatment (NHT) and for the weld with post-welding heat treatment (PWHT) with a 1 kg load. (A) advancing side, (R) retreating side.

different zones of the NHT weld (Fig. 3b) and optical observations of the surface of the electrodes at the end of the polarization tests (Figs. 3c–3e). The same data are given in Figs. 4a–4e for the PWHT weld. Note that all the potentiokinetic polarization curves (Figs. 3b and 4b) present the same overall shape with, at first, a cathodic plateau related to the oxygen reduction reaction. Whatever the zones (BM, HAZ and nugget) and for both weld types (with or without the post welding heat treatment), the cathodic current density was in the range $[6.10^{-5}–10^{-4}]$ A cm^{-2}. All curves presented only one breakdown potential corresponding to the corrosion potential with values in good general agreement with the OCP measurements (Figs. 3a and 4a). For all metallurgical zones, the corrosion potential was followed by a strong increase of the anodic current density. No passivation plateau was observed which showed that all zones, for both samples (NHT and PWHT), were susceptible to corrosion in 1 M NaCl solution at their corrosion potential. Figures 3c–3e show that the corrosion morphology observed after individual electrochemical tests for the NHT samples was pitting corrosion for the base metal (Fig. 3c) and intergranular corrosion for the HAZ (Fig. 3d) and the nugget (Fig. 3e). The HAZ seemed to become more damaged than the other zones which could be related to the higher anodic current densities measured on the current-potential curve (Fig. 3b). The results were in good agreement with OCP measurements since, after OCP tests, the electrode surfaces were found to be corroded. The corrosion morphology observed after OCP measurements was the same as that observed after potentiokinetic polarization tests but the corrosion damage was obviously less extended. TEM observations carried out on samples removed in the base metal zone, the HAZ and the nugget for the NHT weld gave meaningful interpretation of the intrinsic corrosion behavior of each metallurgical zone. For the base metal (Fig. 5a), the absence of intergranular particles combined with the presence of intragranular Al-Cu-Mn particles which can act as cathodic sites were well correlated with the susceptibility to pitting corrosion of the material. In contrast, the HAZ of the NHT joint exhibited a few precipitates (T_1 and other copper-rich precipitates) at grain boundaries, subgrain boundaries and also in the grains (Fig. 5c). The presence of this precipitation, which was not observed in the base metal of the NHT weld, was due to the increase of temperature during the welding process. Some thermal measurements showed that the temperature in the HAZ could be higher than 140°C.[24] Chen and Bhat proposed a Time-Temperature-Precipitation diagram for the 2195 alloy; this alloy is very similar to the 2050 alloy studied here. They showed that, at a temperature of 150°C, T_1 precipitates could be observed in the bulk of the grains and at grain or subgrain boundaries.[7] Concerning the as welded nugget, it exhibited also some T_1 precipitation at the grain boundaries; some AlCuMn and very few T_1 precipitates were observed in the grains (Fig. 5e). This can be explained by the fact that, during the welding

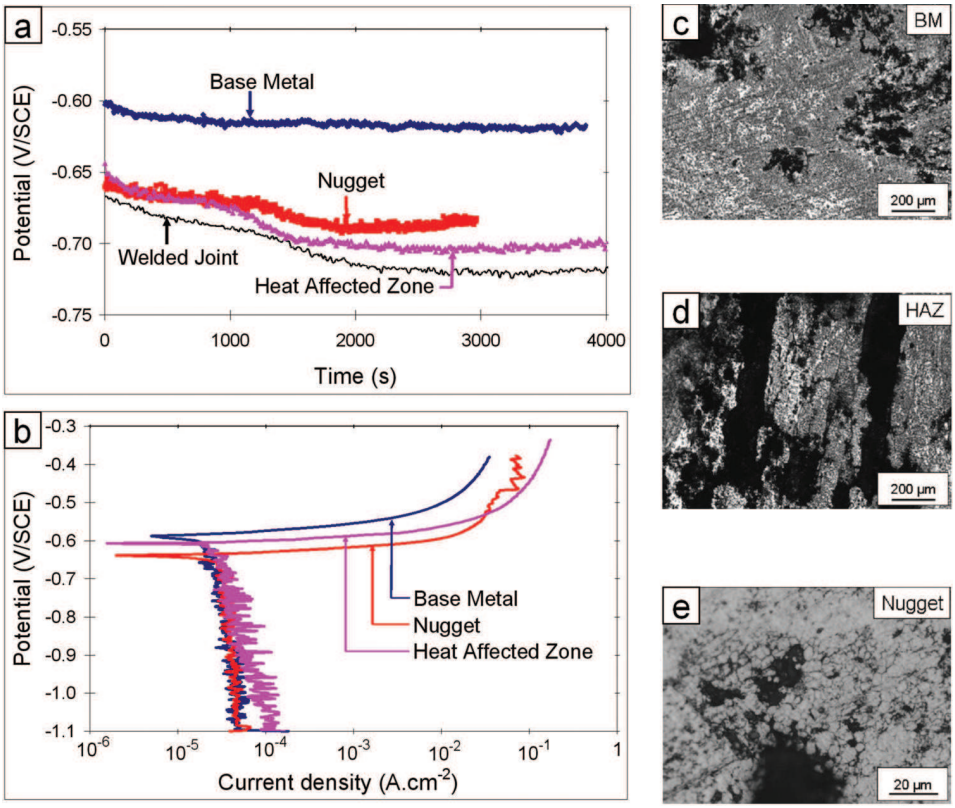

Figure 3. (Color online) (a) OCP measurements (b) current-potential curves in 1M NaCl solution at 22°C for the base metal, the HAZ and the nugget removed from a weld of 2050-T3 alloy without T8 post-welding heat treatment. OCP measurements performed on the global weld are given for comparison. Optical observations of the electrodes after the electrochemical test (c) for the base metal (d) for the HAZ and (e) for the nugget.

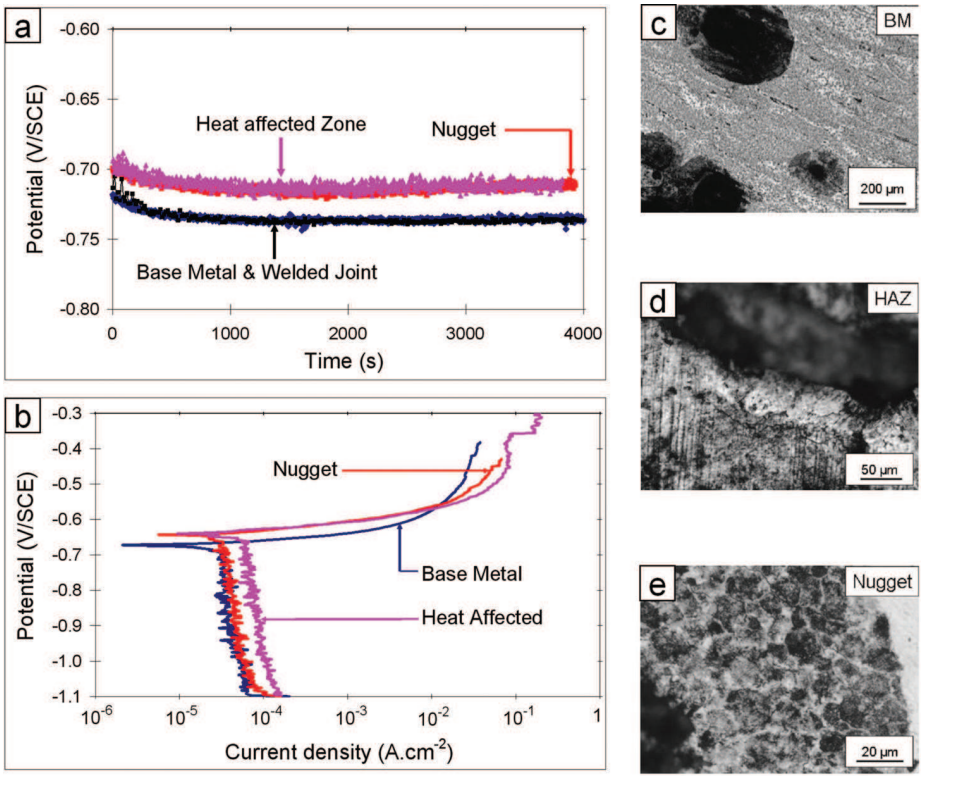

Figure 4. (Color online) (a) OCP measurements (b) current-potential curves in 1 M NaCl solution at 22°C for the base metal, the HAZ and the nugget removed from a weld of 2050-T3 alloy with T8 post-welding heat treatment. OCP measurements performed on the global weld are given for comparison. Optical observations of the electrodes after the electrochemical test (c) for the base metal (d) for the HAZ and (e) for the nugget.

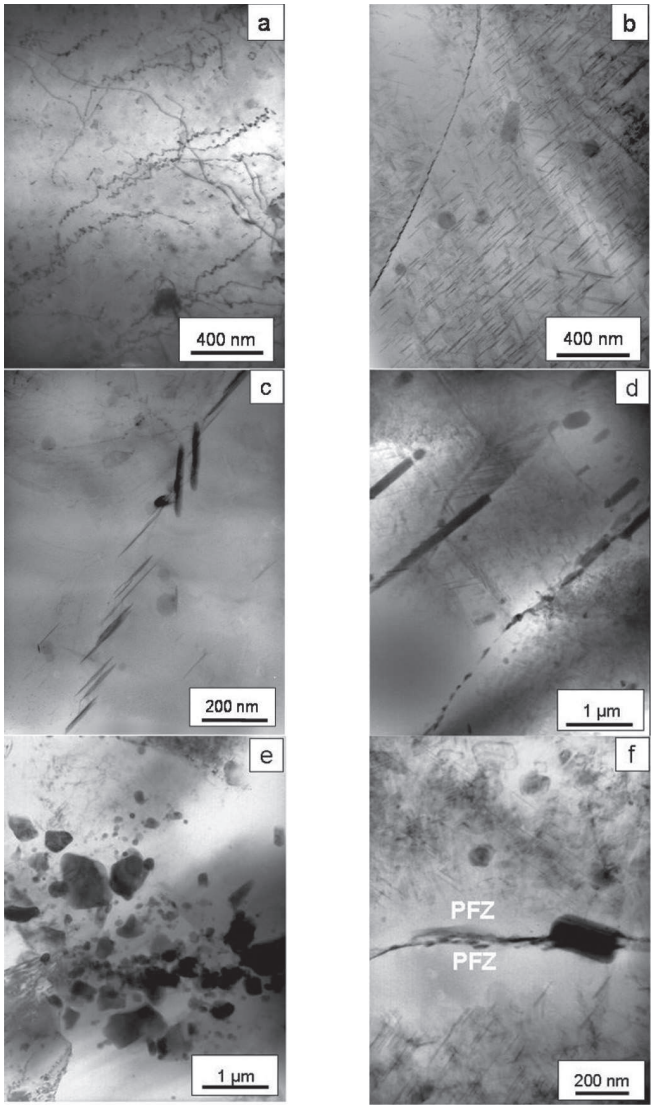

Figure 5. TEM observations of [(a) and (b)] the base metal zone, [(c) and (d)] the HAZ, [(e) and (f)] the nugget of a 2050-T3 FSW joint. Figures [(a), (c), and (e)] correspond to a weld without heat treatment. For figures [(b), (d), and (f)], the weld was submitted to a T8 post-welding heat treatment.

process, due to the recrystallization occurring in the nugget, the dislocation density is not high enough to favor the precipitation of T_1 phase in the grains. The presence of T_1 precipitates at the grain boundaries of both HAZ and nugget of the NHT weld allowed the susceptibility to intergranular corrosion of these zones to be explained. Galvanic coupling between intergranular T_1 precipitates, which have a corrosion potential that is more negative than that of the matrix, and the surrounding matrix promoted the propagation of intergranular corrosion.[11,13,25] Moreover, the strong grain deformation in the HAZ might significantly contribute to increasing the reactivity of the grain boundaries. The corrosion morphology observed on each metallurgical zone after an OCP measurement on the global welded joint in 1 M NaCl solution was similar to that observed when each zone was exposed to 1 M NaCl individually. However, the intergranular corrosion damage of the HAZ was found to be more extended while only a few pits were observed in the base metal. The same observations were performed after a 750-h Mastmaasis Wet Bottom test (Figs. 6a–6c). Figure 6a showed that the NHT base metal presented a susceptibility to pitting corrosion while, for the HAZ (Fig. 6b) and the nugget (Fig. 6c), intergranular corrosion was observed with extensive propagation of corrosion in the HAZ. The result could be explained by galvanic coupling between the different zones of the welded joint. OCP measurements showed that, for the NHT samples, the HAZ presented the most cathodic OCP which could be related to its microstructure (Fig. 3a). Indeed, while Fig. 5a revealed the absence of both T_1 and θ' hardening precipitates in the base metal of the NHT weld, Fig. 5c showed T_1 precipitates in the HAZ grains. Of course, the corrosion potential of the grain itself depended on the T_1 precipitation rate inside the grain much more than on the T_1 precipitation at the grain boundaries which mainly affects the corrosion behavior of the matrix directly surrounding the grain boundaries (i.e. the PFZ). Indeed, when T_1 precipitates form in the grain, they induce a shift of the grain corrosion potential to more cathodic values since they present a very negative corrosion potential.[25] Microgalvanic effects between T_1 precipitates and the aluminum solid solution thus have to be taken into account here. At the same time, as T_1 precipitation occurs in the grain, the aluminum solid solution contains less copper which also contributes to the shift of the grain corrosion potential to more cathodic potentials. The corrosion potential of the whole HAZ depends on the corrosion potential of the HAZ grain but also on the corrosion potential of the HAZ grain boundaries/intergranular precipitates. Microgalvanic effects have to be taken into account again to explain the corrosion potential of a material such as the HAZ. Due to the larger area of the grain compared to that of the grain boundaries/intergranular precipitates, the HAZ corrosion potential was largely influenced by the HAZ grain corrosion potential. T_1 precipitation in the HAZ grain could thus explain the cathodic corrosion potential measured for the HAZ compared to that of the base metal of the same alloy. Concerning the nugget, the same explanation might be suggested since T_1 precipitation was also observed in the nugget grain even though to a lesser extent. As a consequence, the OCP of the base metal in the NHT sample was more anodic than both the HAZ and the nugget so, when the global welded joint was exposed to a corrosive environment, galvanic coupling occurred between its different parts. The HAZ and the nugget were overall anodically polarized. This led to increased corrosion damage of the HAZ and the nugget in the welded joint by comparison to what was observed when each zone was individually exposed to the electrolyte.

Figures 4c–4e showed that the corrosion morphologies observed in each zone of the PWHT sample after potentiokinetic polarization tests were the same as those obtained in NHT joint with pitting corrosion for the base metal and intergranular corrosion for the HAZ and the nugget. TEM observations showed that numerous T_1 precipitates were observed at the grain boundaries and in the grains for the base metal of the PWHT weld due to the heat treatment (Fig. 5b). θ' precipitates were also observed in the grains. The extended T_1 precipitation in the base metal grain of the PWHT joint was well-correlated with the high hardness measured compared to that of the base metal grain of the NHT joint (Fig. 2). As explained before, T_1 precipitation in the grain induced a shift of the grain corrosion potential towards more cathodic values. Here, T_1 precipitation was so extended, as shown by the hardness value, that it was assumed that the grain corrosion potential could be close to that of the grain boundaries in spite of the presence of T_1 precipitates at the grain boundaries. No susceptibility to intergranular corrosion was thus observed for the base metal of the PWHT joint. Concerning the HAZ of the PWHT joint, extensive precipitation was also observed with T_1 and θ' precipitates in the grains and both copper-rich precipitates and T_1 precipitates at the grain boundaries leading to the formation of a Precipitate Free Zone (PFZ) (Fig. 5d). The nugget exhibited extensive precipitation of hardening phases as well as numerous precipitates in the grain boundaries leading to the appearance of a PFZ confirmed by EDX analyses which highlighted the copper depletion at grain boundaries (Fig. 5f). For the HAZ and the nugget, T_1 precipitation in the grain was less extensive than in the base metal which was also shown by the lower hardnesses measured in these parts (Fig. 2). The grain corrosion potential in these zones was thus less cathodic than for the base metal so galvanic coupling between the grains and the grain boundaries was efficient; this galvanic coupling was enhanced by the presence of a PFZ formed due to a large intergranular precipitation. The observations were in good

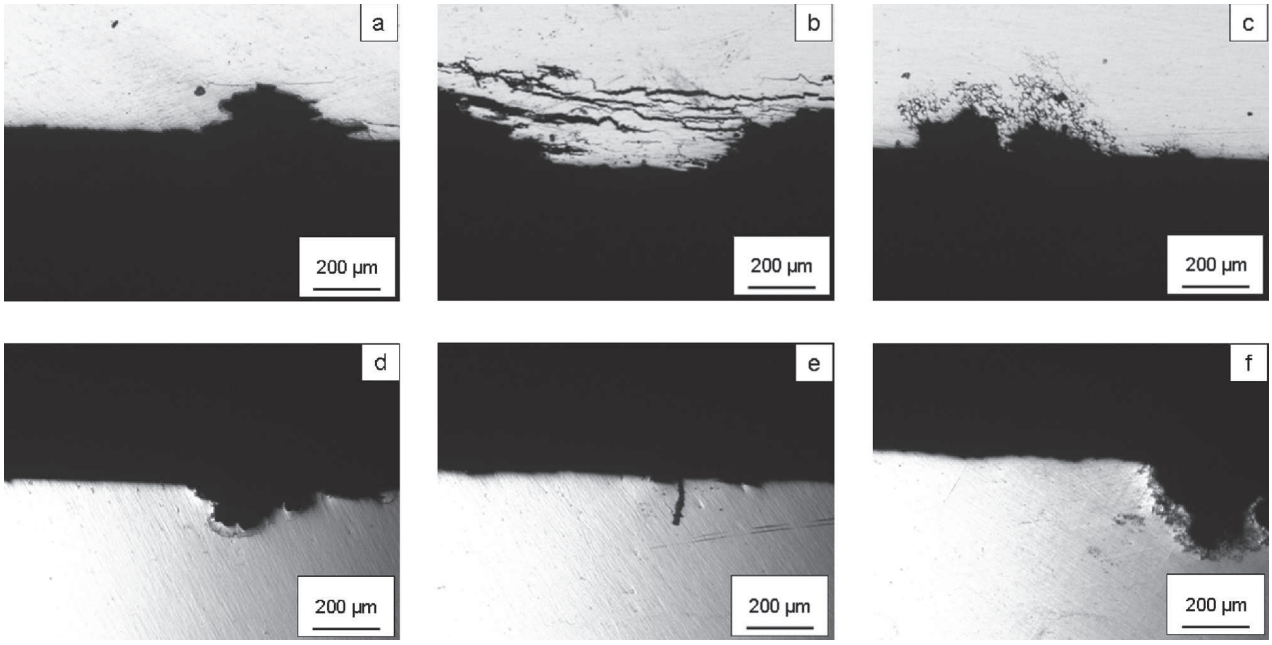

Figure 6. Optical observations of (a) the base metal zone (b) the HAZ and (c) the nugget of a FSW joint of 2050-T3 alloy (d) the base metal zone (e) the HAZ and (f) the nugget of a FSW joint in 2050-T3 alloy with T8 post-welding heat treatment after a 750-h Mastmaasis Wet Bottom test.

agreement with the susceptibility to intergranular corrosion observed for the two zones. Concerning the nugget of the PWHT sample for example, Fig. 4e clearly revealed intergranular corrosion related to the presence of the PFZ. Another consequence of the extended T_1 precipitation in the base metal grain of the PWHT joint was the significant shift towards more cathodic values of its corrosion potential. Figure 4a revealed that the main effect of the T8 post-welding heat treatment concerned the OCP of the base metal. Actually, the OCP measured individually for the base metal became significantly more cathodic for the PWHT sample decreasing from –610 mV/SCE for the NHT sample to –730 mV/SCE for the PWHT sample while, for the HAZ and the nugget, where T_1 precipitation was less extensive, the OCP values varied only between –670 and –710 mV/SCE for the NHT and PWHT samples respectively. Therefore, when post-welding heat treatment was applied, the OCP measured for the individual base metal zone was more cathodic than those measured individually for the HAZ and the nugget (Fig. 4a). The BM was thus anodically polarized and protected the HAZ and the nugget when the joint was exposed to an aggressive environment. These hypotheses deduced from the OCP measurements were in good agreement with the observations performed on both the global welded joint exposed to 1 M NaCl and the Mastmaasis samples. When the FSW joint was submitted to T8 post-welding heat treatment, its corrosion behavior was significantly improved. The morphology of the corrosion observed in the different zones of the PWHT welded joint was similar to that observed for the NHT joints with pitting corrosion in the base metal (Fig. 6d) and intergranular corrosion in both the HAZ (Fig. 6e) and the nugget (Fig. 6f). However, for the PWHT joint, the HAZ did not exhibit a lot of corrosion damage; the corrosion defect shown in Fig. 6e was the only one observed in the whole HAZ. For the nugget, the depth of the intergranular corrosion damage was similar to that measured in the nugget of the NHT joint. Nevertheless, the corrosion sites were significantly less numerous in the PWHT nugget compared to the NHT nugget. Galvanic coupling could thus at least partially explain why the HAZ was more damaged than the other parts of the weld while the welded joint was not heat treated after the welding process (Fig. 6b). In contrast, the HAZ and the nugget were practically intact in the PWHT weld (Figs. 6e and 6f). Comparison of the OCP measured for each individual zone of the weld and that of the global joint showed that, for both NHT and PWHT samples, the OCP of the whole welded joint was similar to that of the less noble zone of the joint (Figs. 3a and 4a). Note that in both NHT and PWHT samples, the OCP of the global joint was slightly lower than those measured individually on each individual part. This could be related to enhanced corrosion damage of the anodic zone of the weld due to galvanic coupling, i.e. the HAZ and the nugget for the NHT sample and the base metal for the PWHT sample, leading to a variation of the surface of the zones and thus of their corrosion potential.

To go further in the understanding of the galvanic coupling phenomena, additional galvanic coupling tests between the different zones of the weld were performed in 1 M NaCl solution for the NHT and PWHT samples. Different galvanic coupling tests were thus performed: base metal/HAZ for both NHT and PWHT samples (Figs. 7a and 7b respectively) and nugget/HAZ for the same samples (Figs. 8a and 8b respectively). For the base metal/HAZ couple, the ratio of exposed area was about six (surface $area_{BM} = 150\ mm^2$; surface $area_{HAZ} = 25\ mm^2$) to be representative of what was observed on a weld; in the same way, the ratio HAZ/nugget was equal to 1 (surface $area_{HAZ}$ = surface $area_{nugget} = 25\ mm^2$). A galvanic coupling test was composed of two similar cycles. Each cycle was composed of a 10-min step during which the two electrodes were not connected together, which allowed the OCP of each electrode to be measured while a galvanic current equal to 0 was recorded, and a two-hour step during which the electrodes were connected so that a galvanic current was recorded in parallel with the OCP of the couple. Due to the electrical connection, a negative current was related to the dissolution of the second term of the couple. For each galvanic coupling test, the two electrodes were observed using optical microscopy after the test; micrographs of the electrode surface are given in Figs. 7 and 8. Figure 7a confirmed that the OCP of the HAZ was less noble than that of the base metal for the NHT sample so the HAZ was anodically polarized when the two electrodes were electrically connected. The HAZ acted as a sacrificial anode with a galvanic current which had increased in absolute value during the test and reached a value of about – 30 μA at the end of the test. This value corresponded to a current density on the HAZ of –120 $\mu A\ cm^{-2}$. At the end of the galvanic coupling tests, the OCP of the HAZ differed significantly from its initial value which could be due to a strong evolution of the electrode surface due to the corrosion processes. This OCP modification of the HAZ was correlated to a slight

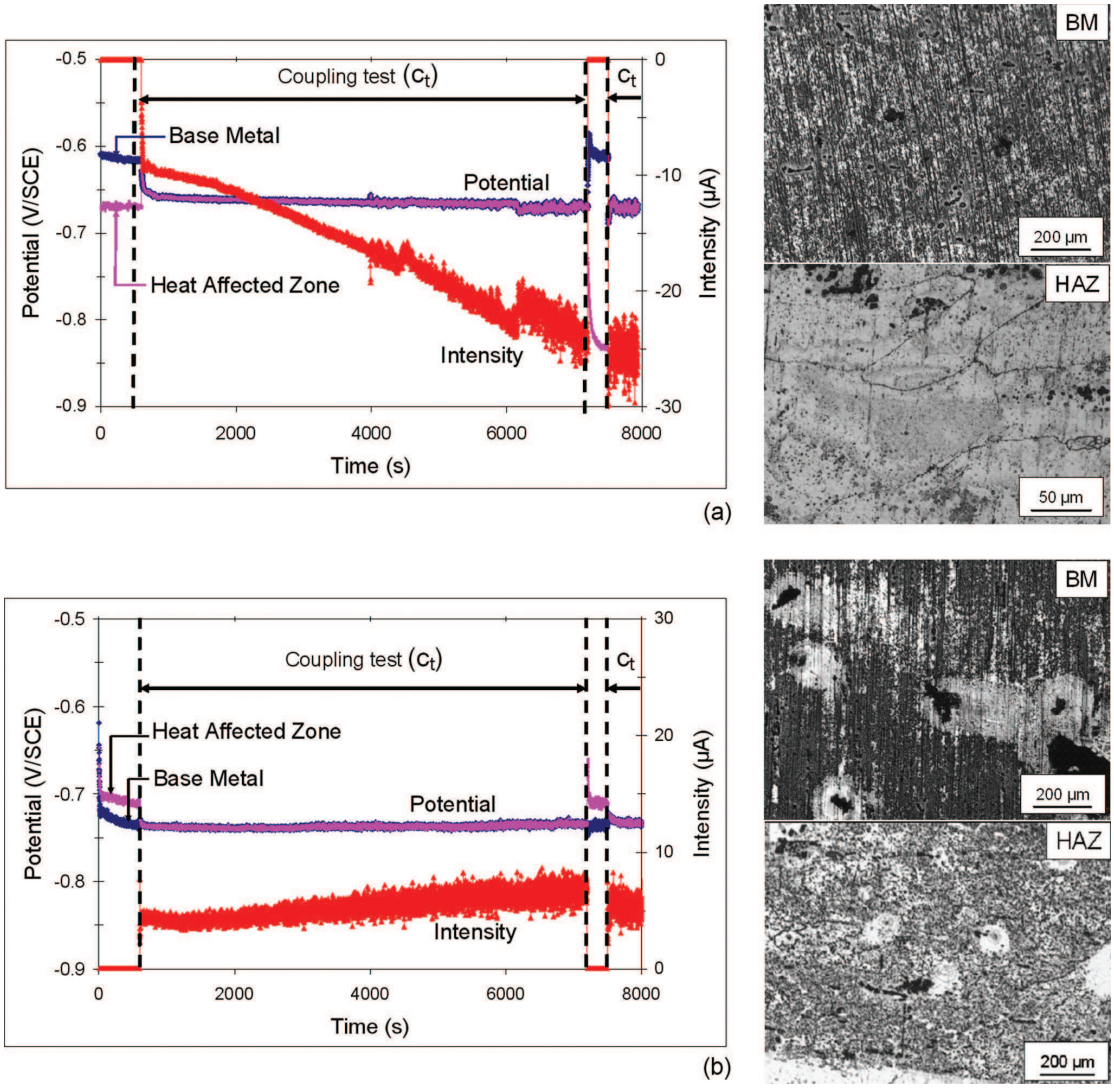

Figure 7. (Color online) Galvanic coupling current measured in 1 M NaCl solution between the base metal and the HAZ of a welded joint of a 2050-T3 alloy. The OCPs of each electrode were measured for 10 min (electrodes disconnected); then the electrodes were electrically connected and the OCP of the couple was measured. Optical observations of the base metal and the HAZ after the galvanic coupling test are given. (a) samples removed from a weld without T8 post-welding heat treatment (b) samples removed from a weld with T8 post-welding heat treatment.

decrease of the OCP of the couple. This is in good agreement with the observation made on the OCP measurements of the global welded joints (Fig. 3a). After the tests, the BM presented pitting corrosion and the HAZ intergranular corrosion, as expected. When a similar test was performed with the base metal and the HAZ removed from the welded joint with a post-welding heat treatment (Fig. 7b), the galvanic current was found to be positive which showed that the BM was now the anode while the HAZ was protected. Table I sums up the values for the different galvanic coupling tests. The galvanic current was here six times weaker, only about 5 μA, compared to that measured in the coupling test between the BM and the HAZ removed from the NHT sample. This value corresponds to a current density of 3 μA cm^{-2} on the base metal. For this experiment, the OCP of the two zones remained constant after the coupling test although the BM was found to be corroded. This could be due to the corrosion morphology observed after the coupling tests. For the base metal, pitting corrosion was observed as expected while the HAZ did not present intergranular corrosion but only a few pits. The results were thus in good agreement with the earlier conclusions, i.e., that the galvanic coupling effect between the base metal and the HAZ can explain the corrosion behavior of the global weld. Due to the T8 post welding heat treatment, the microstructures of the base metal and the HAZ were modified; the corrosion behavior of the base metal was significantly modified while that of the HAZ was slightly affected which led to a modification of galvanic coupling compared to the situation observed on the NHT sample. Furthermore, the low value of the galvanic current measured for the PWHT couple corroborated the enhanced

Table I. Results of galvanic coupling tests.

	BM/HAZ–NHT joint	BM/HAZ–PWHT joint	nugget/HAZ–NHT joint	nugget/HAZ–PWHT joint
Galvanic coupling current (μA)	–30	5	<5	6
Galvanic coupling current density (μA cm^{-2}) on the anode of the couple	–120	3	<20	24

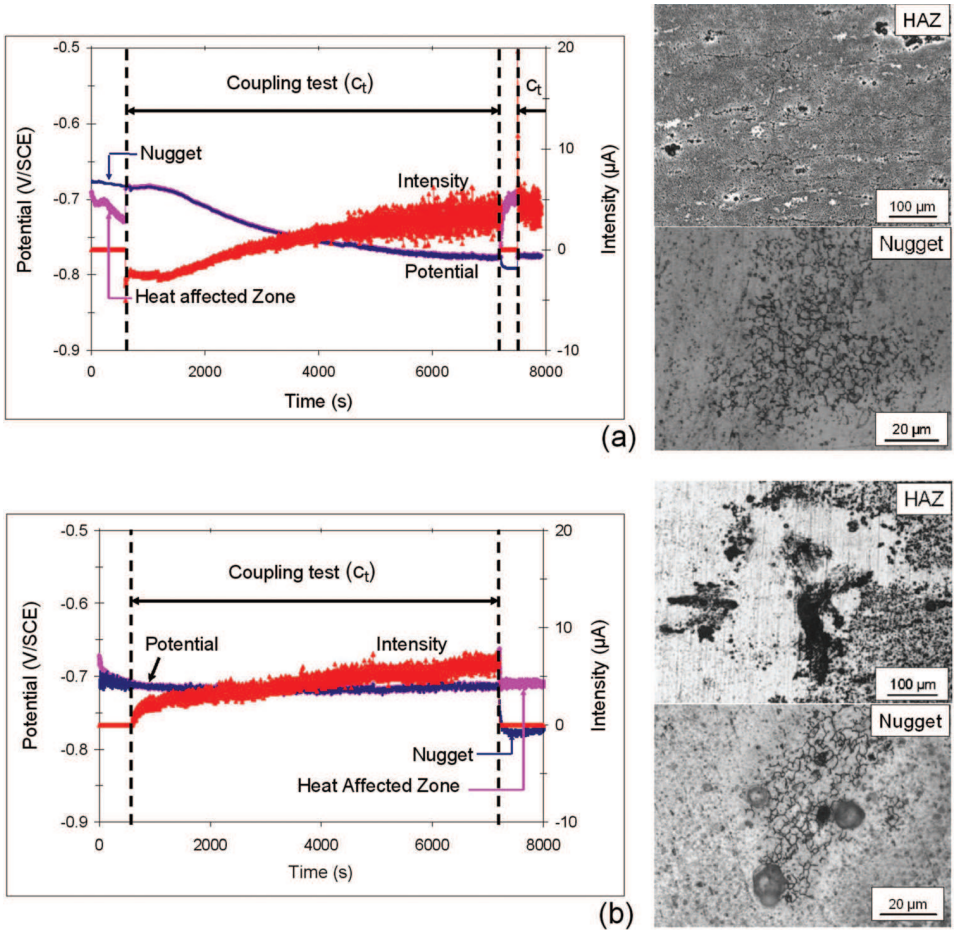

Figure 8. (Color online) Galvanic coupling current measured in 1 M NaCl solution between the nugget and the HAZ of a welded joint of a 2050-T3 alloy. The OCPs of each electrode were measured for 10 min (electrodes disconnected); then the electrodes were electrically connected and the OCP of the couple was measured. Optical observations of the HAZ and the nugget after the galvanic coupling test are given. (a) samples removed from a weld without T8 post-welding heat treatment (b) samples removed from a weld with T8 post-welding heat treatment.

corrosion resistance of the weld after heat treatment. Galvanic coupling between the base metal and the HAZ at least partially explained this. The phenomenon was so efficient that the intrinsic susceptibility to intergranular corrosion of the HAZ, which is due to its microstructure, was no longer visible in the PWHT samples.

OCP measurements and current-potential curves (Figs. 3 and 4) showed that, for both NHT and PWHT samples, the corrosion potentials of the HAZ and of the nugget were not significantly different. It was thus assumed that galvanic coupling effect between these two zones was not as strong as that observed between the HAZ and the base metal. However, galvanic coupling between the HAZ and the nugget was also studied. In the NHT sample (Fig. 8a), the galvanic current was negative at the beginning of the test, which corresponded to the dissolution of the HAZ, and then became positive due to the anodic behavior of the nugget. Whatever the sign of the current, it remained low with a value at the end of the test of under 5 μA which corresponds to a current density of 20 μA cm^{-2}. Comparison with the values measured between the base metal and the HAZ in the NHT sample confirmed that galvanic coupling was greatest between the HAZ and the base metal. After the test, the HAZ and the nugget presented intergranular corrosion as observed when they were immersed individually in 1 M NaCl solution. In PWHT samples, the galvanic current between the nugget and the HAZ was very low at the end of the test, only about 6 μA, which corresponded to a current density of 24 μA cm^{-2} (Fig. 8b). The positive value of the galvanic current indicated that the nugget was being dissolved; at the end of the test, the HAZ did not present intergranular corrosion whereas the nugget did. The HAZ was thus well protected against corrosion by the T8 post-welding heat treatment while pitting was observed in the base metal and intergranular corrosion in the nugget. The results are in good agreement with the previous electrochemical results.

Overall, the results obtained with the galvanic coupling tests confirmed that, for the NHT sample, the corrosion behavior of the weld was mainly related to the galvanic coupling between the base metal and the HAZ leading to an enhanced degradation of the HAZ. When T8 post-welding heat treatment was applied, galvanic coupling between the base metal and the HAZ but also between the HAZ and the nugget led to full protection of the HAZ. Moreover, the galvanic currents were low and even the corrosion damage observed on the base metal and the nugget was not very extensive. The results obtained were in good agreement with the previous electrochemical experiments.

Conclusions

The present study allowed the corrosion behavior of a FSW joint in a 2050-T3 alloy to be studied and related to the microstructure observed. The results demonstrated the efficiency of a T8 post-welding heat treatment as a solution for corrosion protection. The corrosion behavior of the weld was at least partially explained by the galvanic coupling noted between the different parts of the joint. The main effect of the T8 post-welding heat treatment was to significantly change the corrosion behavior of the base metal leading to an inversion in the galvanic coupling phenomena.

Acknowledgments

This work was financially supported by the ANR MatetPro program (ANR-08-MAPR-0020-05). The authors thank C. Henon (Alcan) and M.-C. Lafont (CIRIMAT) for their help.

The authors assisted in meeting the publication costs of this article.

References

1. C. Meric, *Mater. Res. Bull.*, **35**, 1479 (2000).
2. Ph. Lequeu, R. Muzzolini, J. C. Ehrstrom, F. Bron, and R. Maziarz, in *Aeromat*, Seattle, WA (2006).
3. W. M. Thomas, E. D. Nicholas, J. C. Needham, M. G. Murch, P. Templesmith, and C. J. Dawes, International Pat. Appl., PCT/GB92/02203 (1991).
4. B.-P. Huang and Z.-Q. Zheng, *Scr. Mater.*, **38**, 357 (1998).
5. W. A. Cassada, G. J. Shiflet, and E. A. Starke Jr., *Metall. Mater. Trans. A*, **22A**, 287 (1991).
6. B. M. Gable, A. W. Zhu, A. A. Csontos, and E. A. Starke Jr., *J. Light Met.*, **1**, 1 (2001).
7. P. S. Chen and B. N. Bhat, Time-Temperature-Precipitation Behavior in AI-Li Alloy 2195, NASA/TM 2002-211548 (2002).
8. J. F. Li, W. J. Chen, X. S. Zhao, W. D. Ren, and Z. Q. Zheng, *Trans. Nonferrous Met. Soc. China*, **16**, 1171 (2006).
9. B. J. Connolly and J. R. Scully, *Scr. Mater.*, **42**, 1039 (2000).
10. H. Y. Li, Y. Tang, Z. D. Zeng, and F. Zheng, *Trans. Nonferrous Met. Soc. China*, **18**, 778 (2008).
11. J. F. Li, C. X. Li, Z. W. Peng, W. J. Chen, and Z. Q. Zheng, *J. Alloy Compd.*, **460**, 688 (2008).
12. J. F. Li, S. C. Li, W. J. Chen, X. S. Zhao, W. D. Ren, and Z. Q. Zheng, *Trans. Nonferrous Met. Soc. China*, **16**, 1268 (2006).
13. J. F. Li, Z. Q. Zheng, N. Jiang, and S. C. Li, *Mater. Corros.*, **56**, 192 (2005).
14. A. K. Shukla and W. A. Baeslack, *Scr. Mater.*, **56**, 513 (2007).
15. R.W. Fonda and J. F. Bingert, *Metall. Mater. Trans. A*, **37A**, 3593 (2006).
16. O. Hatamleh, P. M. Singh, and H. Garmestani, *J. Mater. Eng. Perform.*, **18**, 406 (2009).
17. J. Corral, E. A. Trillo, Y. Li, and L. E. Murr, *J. Mater. Sci. Lett.*, **19**, 2117 (2000).
18. W. Hu and E. I. Meletis, *Mater. Sci. Forum*, 331–337, 1683 (2000).
19. C. S. Paglia and R. G. Buchheit, *Scr. Mater.*, **58**, 383 (2008).
20. B. N. Padgett, C. Paglia, and R. G. Buchheit, in *Friction Stir Welding and Processing II*, K. V. Jata, M. W. Mahoney, R. S. Mishra, S. L. Semiatin, and T. Lienert, Editors, p. 55, TMS, San Diego (2007).
21. M. D. Danford and R. J. Ding, A Study of Friction Stir Welded 2195 Al-Li Alloy by the Scanning Reference Electrode Technique, NASA/TP-1998-207399, Marshall Space Flight Center, AL (1998).
22. ASTM G85-02, Standard practice for modified salt spray (fog) testing (2003).
23. K. V. Jata and S. L. Semiatin, *Scr. Mater.*, **43**, 743 (2000).
24. M. Jariyaboon, A. J. Davenport, R. Ambat, B. J. Connolly, S. W. Williams, and D. A. Price, *Corros. Sci.*, **49**, 877 (2007).
25. R. G. Buchheit, J. P. Moran, and G. E. Stoner, *Corrosion*, **50**, 120 (1994).